Monostatic DMG Passive Sensing with Hypothesis Testing

Wang, Pu; Boufounos, Petros T.

Abstract

This paper considers object detection with millimeter-wave (mmWave) Wi-Fi beam training frames, e.g., beacon frames, in a monostatic passive directional multi-gigabit (DMG) sensing configuration. We derive an explicit signal model that accounts for the preamble, frame-to-frame antenna gains, and clutter. Given the signal model, we develop a hypothesis testing-based object detection that directly leverages symbol-level preamble waveforms and explores the Kronecker structure between the range steering vector and the Doppler steering vector weighted by the antenna gain. Numerical results confirm the effectiveness of the proposed detector and evaluate the impact of frame-to-frame antenna gains due to the beam scanning.

MONOSTATIC DMG PASSIVE SENSING WITH HYPOTHESIS TESTING

Pu Wang and Petros Boufounos

Mitsubishi Electric Research Laboratories (MERL)
Cambridge, MA 02139, USA

ABSTRACT

This paper considers object detection with millimeter-wave (mmWave) Wi-Fi beam training frames, e.g., beacon frames, in a monostatic passive directional multi-gigabit (DMG) sensing configuration. We derive an explicit signal model that accounts for the preamble, frame-to-frame antenna gains, and clutter. Given the signal model, we develop a hypothesis testing-based object detection that directly leverages symbol-level preamble waveforms and explores the Kronecker structure between the range steering vector and the Doppler steering vector weighted by the antenna gain. Numerical results confirm the effectiveness of the proposed detector and evaluate the impact of frame-to-frame antenna gains due to the beam scanning.

Index Terms— Wi-Fi sensing, Directional Multi-Gigabit (DMG), beam training, WLAN Sensing, 802.11bf, passive sensing.

1. INTRODUCTION

Wi-Fi has become an integral part of our daily lives, serving as the backbone for communication, entertainment, remote working, virtual reality, industry-level IoT, and social connectivity. With the massive deployment of Wi-Fi devices and anticipated market growth, enabling sensing functionalities to future Wi-Fi technologies has attracted interest from academia and industry.

In on-going IEEE 802.11bf WLAN Sensing standard developments, Wi-Fi sensing can be categorized into *sub-7-GHz Wi-Fi sensing* and *directional multi-gigabit (DMG) Wi-Fi sensing* at frequencies over 45 GHz [1–4]. At a typical range of 10 meters, Wi-Fi signal at 60 GHz may experience an additional 22-dB attenuation over the propagation loss at 5 GHz [5–8]. Therefore, it is critical to use directional beamforming to compensate for such a large path loss. As a unique feature of 802.11ad/ay, DMG beam training is usually initiated by the AP during the beacon transmission interval (BTI), where directional frames are transmitted over sector-level beampatterns to probe the environment; see Step 1 of Fig. 1(a). Multiple users can simultaneously compute their own received beam SNRs corresponding to each of the transmitted beampatterns and identify their respective best beam for downlink data transmission. In the subsequent association beamforming training (A-BFT), users can train its beampatterns by sending directional frames to the AP; see Step 2 of Fig. 1(a). Once the best pair of downlink-uplink beampatterns are identified, high-throughput data transmission then follows during data transmission interval (DTI); see Step 3 of Fig. 1(a).

Assuming full-duplex operation with sufficient self-interference cancellation [9,10], repurposing DMG Wi-Fi frames for sensing was first studied in [11, 12], where the Golay sequence-based preamble including short training field (STF) and channel estimation field (CEF), of single-carrier physical layer (SCPHY) data frames in Step 3 of Fig. 1(a). [13] proposed a modified Doppler-resilient Golay sequence for robust performance particularly on detecting moving ob-
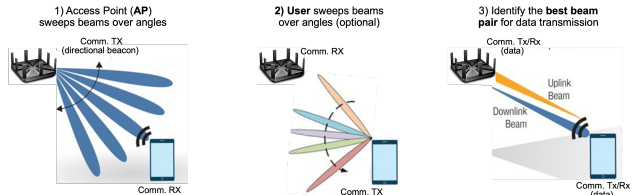
(a) DMG beam training in 802.11ad/ay for data transmission
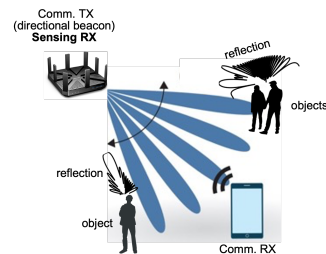
(b) Monostatic DMG passive sensing

Fig. 1: Existing DMG beam training (a) in 802.11 ad/ay and monostatic DMG passive sensing (b) that reuses the same beacon frames for sensing.

jects. Beam training measurements at earlier stages (Steps 1 and 2 of Fig. 1(a)) were also considered for sensing. [14] proposed to reuse the control PHY (CPHY) frames during BTI and/or A-BFT sector-level beam training intervals. and utilized the generalized likelihood ratio test (GLRT) to detect single object from noise. This was further extended in [15] to handle the presence of multiple objects and [16] with a subspace approach over the delay-Doppler domain. However, this frame-to-frame TX-RX antenna gain introducing additional phase change on top of the Doppler modulation was not considered in [14–16]. Different from the above studies focusing on outdoor automotive applications, 802.11bf WLAN Sensing considers an optional feature of DMG passive sensing that reuses directional beacon frames within BTI; see Fig. 1(b). Under this setting, [17] utilized traditional communication-based frame detection and channel impulse response (CIR) estimation blocks that rely on the correlation properties of Golay preamble, and adopted the classical MUSIC algorithm for both angle and delay parameter estimation.

In this paper, we are interested in the DMG passive sensing in a monostatic setting where additional sensing RX is deployed at the AP to capture the reflected beacon frames. Explicitly, we account for the frame-to-frame TX-RX antenna gain (due to the misalignment between the probing sector beampatterns and the object steering vector) to the frame-based slow-time samples for Doppler steering vector. We show that the joint TX-RX steering vector has a Kronecker structure between the range-domain steering vector (formed by the delayed preamble matched filter output) and the Doppler steering

vector element-wise weighted by antenna gains. Following that, rather than a sequential approach of , we directly formulate object detection as a binary hypothesis testing where both preamble and Doppler steering vector are utilized. According to the developed signal model, a subspace-based object detector and a computational implementation are proposed according to the principle of generalized likelihood ratio test (GLRT).

2. SIGNAL MODEL

For each beacon frame within the BTI subinterval, the transmitter sends a preamble of length L

$$s_g(t) = \sqrt{E_s} \sum_{l=0}^{L-1} s_l g_{\text{TX}}\left(t - lT_s\right), \tag{1}$$

where E_s is the symbol energy, s_l is the modulated symbol after $\pi/2$-BPSK modulation with alphabet of $\{\pm 1, \pm i\}$, $g_{\text{TX}}(t)$ is the baseband pulse, and $T_s = 1/B$ is the symbol interval with B denoting the channel bandwidth. Note that $g_{\text{TX}}(t)$ includes the effect of a spectral mask, e.g., a pair of TX and RX filter for error vector magnitude measurement as a root-raised cosine (RRC) filter with a roll-off factor of 0.25, for the transmit waveform to limit inter-symbol interference (ISI).

Consider the upconversion to the carrier frequency f_c, TX analog beamforming angle/sector at θ_k for the k-th packet, and a coherent processing interval of K packets, we have

$$x_T(t) = \sum_{k=0}^{K-1} \mathbf{f}_{\text{TX}}(\theta_k) s_g(t - kT_p) e^{j2\pi f_c t}, \tag{2}$$
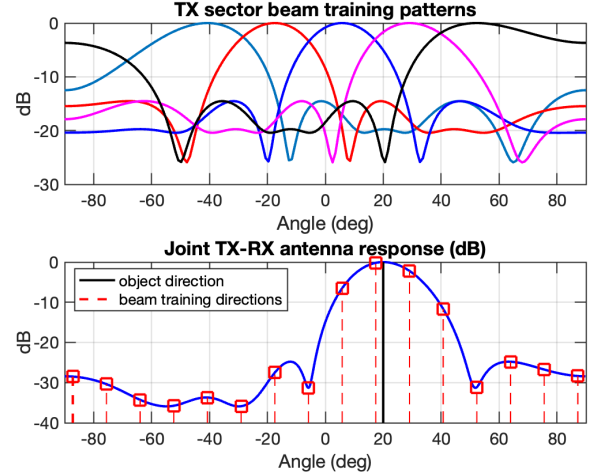
where T_p is the pulse repetition interval (PRI), f_c is the carrier frequency, and $\mathbf{f}_{\text{TX}}(\theta_k)$ is the sector beamforming pattern pointing at θ_k at the k-th frame; see the top plot of Fig. 2 for an illustration of $K = 5$ sector-level (a mainlobe of $30°$) beam scanning.

The monostatic sensing channel is modeled to be a sum of P reflections including both objects of interest and background scatterers such as reflectors from the wall, ground, ceiling and furniture. For each reflection, we parameterize its sensing channel using its azimuth (ignoring elevation without losing generality), round-trip delay $\tau_p = 2R_p/c$ with c is the speed of light, small-scale complex-valued channel gain β_p, large-scale channel gain G_p, and Doppler shift $\nu_p = 2v_p/\lambda$ with v_p denoting the radial velocity and $\lambda = c/f_c$ the wavelength. With the colocated TX/RX, we have

$$\mathbf{H}(t) = \sum_{p=1}^{P} \mathbf{H}(t; \tau_p, \theta_p, \nu_p)$$

$$= \sum_{p=1}^{P} \alpha_p e^{j2\pi\nu_p t} \delta(t - \tau_p) \mathbf{s}_{\text{RX}}(\theta_p) \mathbf{s}_{\text{TX}}^{H}(\theta_p), \tag{3}$$

where $\alpha_p = \sqrt{G_p}\beta_p$ with $G_p = \lambda^2 \sigma_{\text{RCS},p}/(64\pi^2 R_p^4)$ and $\sigma_{\text{RCS},p}$ is the RCS corresponding to the p-th object, $\mathbf{s}_{\text{RX}}(\theta_p)$ and $\mathbf{s}_{\text{TX}}(\theta_p)$ are, respectively, the angular channel vector at Tx and Rx. In the case of uniform linear array (ULA) with M transmitting antennas and N receiving antennas, we have

$$\mathbf{s}_{\text{TX}}(\theta) = \frac{1}{\sqrt{M}} \left[1, e^{j2\pi f_{\text{TX}}(\theta)}, \cdots, e^{j2\pi(M-1)f_{\text{TX}}(\theta)}\right],$$

$$\mathbf{s}_{\text{RX}}(\theta) = \frac{1}{\sqrt{N}} \left[1, e^{j2\pi f_{\text{RX}}(\theta)}, \cdots, e^{j2\pi(N-1)f_{\text{TX}}(\theta)}\right], \tag{4}$$

Fig. 2: Top: An example of $K = 5$ sector-level beamforming patterns at TX; Bottom: joint TX-RX antenna gains for $K = 16$ beam directions (red lines) for an object-of-interest at 20 degree (black line).

where $f_{\text{TX}}(\theta) = d_t \sin(\theta)/\lambda$ and $f_{\text{RX}}(\theta) = d_r \sin(\theta)/\lambda$. With the analog receiver combining at k-th frame interval $\mathbf{f}_{\text{RX}}(\theta_k)$, the tap-delay channel response is given as

$$\mathbf{h}(t, \tau, \theta_k) = \sum_{p=1}^{P} \mathbf{f}_{\text{RX}}^{H}(\theta_k)\mathbf{H}(t; \tau_p, \theta_p, \nu_p)\mathbf{f}_{\text{TX}}(\theta_k)$$

$$= \sum_{p=1}^{P} a_p(\theta_k)e^{j2\pi\nu_p t}\delta(t - \tau_p) \tag{5}$$

where $a_p(\theta_k) = \alpha_p s_k(\theta_p) = a_p \mathbf{f}_{\text{RX}}^{H}(\theta_k)\mathbf{s}_{\text{RX}}(\theta_p)\mathbf{s}_{\text{TX}}^{H}(\theta_p)\mathbf{f}_{\text{TX}}(\theta_k)$ is the effective amplitude of the p-th object for the k-th packet. In the bottom plot of Fig. 2, we show the joint TX-RX antenna gain $s_k(\theta_p)$ when $K = 16$ sector-level beam scanning patterns are used and the object-of-interest is at $\theta_p = 20$ degree. It is seen that only the beam sector closing to the object yields strong antenna gains, while other beam sectors may give an antenna gain of -30 dB. For all $K = 16$ beacon frames, the frame-to-frame antenna gain fluctuation results in not only the effective SNR changes per frame but also the phase modulation over frames.

At the receiver side, the analog combined signal for the k-th packet is given as $y_k(t) = \sum_{p=1}^{P} a_p(\theta_k)e^{j2\pi\nu_p t}s_g(t - \tau_p)$. Then the combined signal is matched filtered with $g_{\text{RX}}(t)$ as

$$r_k(t) = y_k(t) * g_{\text{RX}}(t) = \sum_{p=1}^{P} a_p(\theta_k)[e^{j2\pi\nu_p t}s_g(t - \tau_p)] * g_{\text{RX}}(t)$$

$$\times g_{\text{TX}}\left(t - lT_s - \tau_p - z\right) dz$$

$$\approx \sqrt{E_s} \sum_{p=1}^{P} a_p(\theta_k)e^{2\pi j\nu_p t} \sum_{l=0}^{L-1} s_l \int_{-\infty}^{+\infty} g_{\text{RX}}(z)$$

$$\times g_{\text{TX}}\left(t - lT_s - \tau_p - z\right) dz$$

$$= \sum_{p=1}^{P} \sqrt{E_s} a_p(\theta_k)e^{2\pi j\nu_p t}x_g(t - lT_s - \tau_p) \tag{6}$$

where the approximation holds due to the fact that the relative Doppler shift ν_p is much smaller than the bandwidth $B = 1.76$ GHz,

$x_g(t - \tau_p) = \sum_{l=0}^{L-1} s_l g(t - lT_s - \tau_p)$ is the matched filter output for the preamble of the p-th packet, and $g(t - \tau) = g_{\text{TX}}(t - \tau) * g_{\text{RX}}(t)$ is the matched pulse shaping at a given delay.

The analog signal is then sampled at $t = kT_p + nT_s$, where T_s and T_p are, respectively, the fast-time and slow-time sampling intervals. The discrete-time representation of the received signal is given as

$$y[n, k] = y(t)_{t=kT_p+nT_s}$$
$$= \sqrt{E_s} \sum_{p=1}^{P} a_p(\theta_k) e^{j2\pi\nu_p(kT_p+nT_s)} x_g(nT_s - \tau_p)$$
$$\approx \sqrt{E_s} \sum_{p=1}^{P} a_p(\theta_k) e^{j2\pi\nu_p kT_p} x_g(nT_s - \tau_p) \quad (7)$$

where $x_g(nT_s - \tau_p) = x_g((kT_p + nT_s) - \tau_p)$ and the approximation holds by assuming a standard motion speed of indoor object and its negligible effect on the phase.

Grouping all the fast-time samples (n) first and then the slow-time sample (k), we have the following signal model

$$\mathbf{y} = \sqrt{E_s}\alpha_0 [\mathbf{s}_a(\theta_0) \odot \mathbf{s}_d(\nu_0)] \otimes \mathbf{x}_g(\tau_0)$$
$$+ \sum_{p=1}^{P} \sqrt{E_s}\alpha_p [\mathbf{s}_a(\theta_p) \odot \mathbf{s}_d(\nu_p)] \otimes \mathbf{x}_g(\tau_p) + \mathbf{w} \quad (8)$$

where the subindex 0 denotes the object of interest, $\mathbf{s}_a(\theta_p) = [s_1(\theta_p), \cdots, s_K(\theta_p)]^T$ denotes the steering vector of the p-th object responding to the K transmit-receive beam training directions $\{\theta_k\}_{k=0}^{K}$, $\mathbf{s}_d(\nu_p) = [1, \cdots, e^{-j2\pi\nu_p T_p(K-1)}]^T$ denotes the Doppler steering vector of the p-th object, $\mathbf{x}_g(\tau_p)$ is the delay steering vector of the p-th object with a dimension $N \times 1$, and $\mathbf{w} \sim \mathcal{CN}(\mathbf{0}, \sigma^2\mathbf{I}_{NK})$ is the noise. We consider the scenario that all other reflections ($p \neq 0$) from the indoor environment such as wall, ceiling, ground, furniture construct the background clutter. Particularly, we assume the clutter-related path delays (τ_p) and angles (θ_p) stay the same but their amplitudes $[\alpha_1, \cdots, \alpha_P]^T \sim \mathcal{CN}(\mathbf{0}, \mathbf{C}_P)$ are random with a covariance distribution $\mathbf{C}_P$.

From (8), it is seen that the object steering vector has a Kronecker structure between the slow-time and the fast-time. It is interesting to see that, sine the beam training in the DMG passive sensing is designed for later data transmission, the mismatch between the transmit-receive beam direction and the object direction results in additional slow-time phase perturbation on top of the slow-time Doppler modulation. As a result, the problem of interest is to detect the object of interest from the environmental clutter and noise.

3. JOINT RANGE-ANGLE-DOPPLER ADAPTIVE DETECTION FOR MONOSTATIC DMG PASSIVE SENSING

Given the above signal model of (8), we develop a joint range-angle-Doppler (RAD) adaptive detector for DMG passive sensing.

3.1. Hypothesis Testing

To formulate the binary hypothesis test we consider the object signal, and the disturbance including the background clutter and thermal noise. More specifically,

$$H_0 : \mathbf{y} = \mathbf{Hc} + \mathbf{w},$$
$$H_1 : \mathbf{y} = \alpha\mathbf{s}_{rad} + \mathbf{Hc} + \mathbf{w}, \quad (9)$$

where $\mathbf{s}_{rad} = [\mathbf{s}_a(\theta_0) \odot \mathbf{s}_d(\nu_0)] \otimes \mathbf{s}_r$ is the object angle-Doppler steering vector to be tested at a given angle-Doppler grid (θ_0, ν_0), $\mathbf{s}_r = \mathbf{x}_g(\tau_0)$ is the range steering vector at the delay τ_0, the background clutter steering matrix is given as

$$\mathbf{H} = [\mathbf{s}_{sad}(\tau_1, \theta_1, \nu_1), \cdots, \mathbf{s}_{rad}(\tau_P, \theta_P, \nu_P)] \in \mathbb{C}^{NK \times P} \quad (10)$$

with corresponding clutter coefficient $\mathbf{c} = [\alpha_1, \cdots, \alpha_P]^T \in \mathbb{C}^{P \times 1}$, and the noise $\mathbf{w}$. Note that, due to the sparse channel characteristics at the mmWave frequency bands, we have $P \ll NK$.

In addition to the test signal $\mathbf{y}$, we also assume training signals $\mathbf{y}_t$ that are object-free and the range-angle-Doppler parameters $(\theta_p, \tau_p, \nu_p)_{p=1}^{P}$ for each clutter component remain the same. However, the clutter coefficients $\mathbf{c}_t$ and the noise variance σ^2 vary from the training data to the test data. For instance, in the context of DMG passive sensing, the object-free training signals can be collected when there are no presence of the object of interest in the environment. Given this assumption, one can use the training data to estimate the channel parameters $(\theta_p, \tau_p, \nu_p)_{p=1}^{P}$ of the clutter. As a result, $\mathbf{H}$ is known in advance and $\mathbf{c}$ is unknown but deterministic.

3.2. Joint Range-Angle-Doppler Detection

Given a known Clutter steering matrix $\mathbf{H}$, the unknown parameters are the object amplitude α_0, the clutter coefficient $\mathbf{c}$, the noise variance σ^2 under H_1 and the clutter coefficient $\mathbf{c}$, the noise variance σ^2 under H_0. The GLRT can be derived as the ratio of maximized likelihoods under the two hypotheses

$$T = \frac{\max_{\alpha_0, \mathbf{c}, \sigma^2} f_1(\mathbf{y} \,|\, \alpha, \mathbf{c}, \sigma^2)}{\max_{\mathbf{c}, \sigma^2} f_0(\mathbf{y} | \mathbf{c}, \sigma^2)}, \quad (11)$$

where T is the test statistic, and $f_0(\mathbf{y}|\sigma^2)$ and $f_1(\mathbf{y}|\alpha, \boldsymbol{\eta}, \sigma^2)$ are, respectively, the likelihood functions of the whitened signal

$$f_{0|1}(\mathbf{y} \,|\, \alpha, \mathbf{c}, \sigma^2) = \frac{e^{-\frac{1}{\sigma^2}\|\mathbf{y} - \alpha\mathbf{s}_{rad} - \mathbf{Hc}\|^2}}{(\pi\sigma^2)^{NK}} \Big|_{\alpha=0|\alpha\neq0}.$$

By differentiating $\ln f_1(\mathbf{y} \,|\, \alpha, \boldsymbol{\eta}, \sigma^2)$ w.r.t. σ^2 and setting to zero, the ML estimate of σ^2 under H_1

$$\hat{\sigma}_1^2 = \frac{1}{NK}\|\mathbf{y} - \alpha\mathbf{s}_{rad} - \mathbf{Hc}\|^2. \quad (12)$$

Then it is equivalent to minimizing the following cost function for the clutter coefficient $\mathbf{c}$: $\|\bar{\mathbf{y}}_{0|1} - \mathbf{Hc}\|^2$, where $\bar{\mathbf{y}}_{0|1} = (\mathbf{y} - \alpha\mathbf{s}_{rad})|_{\alpha=0|\alpha\neq0}$, which leads to

$$\hat{\mathbf{c}} = (\mathbf{H}^H\mathbf{H})^{-1}\mathbf{H}^H\bar{\mathbf{y}}_{0|1}. \quad (13)$$

Substituting $\hat{\mathbf{c}}$ back to the cost function, we have the following cost function (ignoring the constant $1/(NK)$)

$$\bar{\mathbf{y}}_{0|1}^H \mathbf{P}_{\mathbf{H}}^{\perp}\bar{\mathbf{y}}_{0|1} = \begin{cases} (\mathbf{y} - \alpha_0\mathbf{s}_{rad})^H \mathbf{P}_{\mathbf{H}}^{\perp}(\mathbf{y} - \alpha_0\mathbf{s}_{rad}) & \text{under } H_1 \\ \mathbf{y}^H\mathbf{P}_{\mathbf{H}}^{\perp}\mathbf{y} & \text{under } H_0 \end{cases}$$
$$(14)$$

where $\mathbf{P}_{\mathbf{H}}^{\perp} = \mathbf{I} - \mathbf{H}(\mathbf{H}^H\mathbf{H})^{-1}\mathbf{H}^H$ is the projection matrix to the orthogonal complement of the range of clutter steering matrix $\mathbf{H}$. As a result, the object amplitude under H_1 can be estimated as

$$\hat{\alpha}_0 = \frac{\mathbf{s}_{rad}^H\mathbf{P}_{\mathbf{H}}^{\perp}\mathbf{y}}{\mathbf{s}_{rad}^H\mathbf{P}_{\mathbf{H}}^{\perp}\mathbf{s}_{rad}}. \quad (15)$$

And the cost function under H_1 reduces to

$$\mathbf{y}^H \mathbf{P}_{\tilde{\mathbf{H}}}^{\perp} \mathbf{y} - \frac{\|\mathbf{s}_{rad}^H \mathbf{P}_{\tilde{\mathbf{H}}}^{\perp} \mathbf{y}\|^2}{\mathbf{s}_{rad}^H \mathbf{P}_{\tilde{\mathbf{H}}}^{\perp} \mathbf{s}_{rad}}. \qquad (16)$$

Putting the likelihood back to the GLRT in (11) and invoking the monotonic property of the function $f(x) = 1/(1-x)$, we have

$$T = \frac{\|\mathbf{s}_{rad}^H \mathbf{P}_{\tilde{\mathbf{H}}}^{\perp} \mathbf{y}\|^2}{(\mathbf{s}_{rad}^H \mathbf{P}_{\tilde{\mathbf{H}}}^{\perp} \mathbf{s}_{rad})(\mathbf{y}^H \mathbf{P}_{\tilde{\mathbf{H}}}^{\perp} \mathbf{y})} \qquad (17)$$

It is seen that the joint RAD detector takes the ratio of the energy of the clutter-free signal projected onto a subspace and its orthogonal complement, where the subspace is spanned by the Kronecker product of the column space of whitened transmitting steering vector $\tilde{\mathbf{s}}$ and the whitened subspace $\tilde{\mathbf{H}}_t$ for the waveform residuals.

3.3. Non-coherent Combining of Partial-Preamble-Based RAD Detection

It is noted that the joint range-angle-Doppler steering vector $\mathbf{s}_{rad}$ is of dimension $KN \times 1$ where $K \ll N$. In the case of DMG beacon-based beam training, $K = 128$ and $N = 7752$, resulting in $KN \approx$ 1e+6 and the fully adaptive joint RAD detector (19) is not computationally affordable. Alternatively, we propose to decompose the range steering vector $\mathbf{s}_r$ into small segments each corresponding to a segment of preamble matched filter output with a proper delay under test.

$$\begin{aligned} H_0 &: \ \mathbf{y}_i = \mathbf{H}_i \mathbf{c}_i + \mathbf{w}_i, \\ H_1 &: \ \mathbf{y}_i = \alpha \mathbf{s}_{rad,i} + \mathbf{H}_i \mathbf{c}_i + \mathbf{w}_i, \end{aligned} \qquad (18)$$

where $\mathbf{s}_{rad,i} = [\mathbf{s}_a(\theta_0) \odot \mathbf{s}_d(\nu_0)] \otimes \mathbf{s}_{r,i}$ is the object range-angle-Doppler steering vector to be tested at a given angle-Doppler grid (θ_0, ν_0) and the partial-preamble range steering vector $\mathbf{s}_{r_i} = \mathbf{x}_{g,i}(\tau_0)$. And the non-coherent combination of partial-preamble RAD detection is given as

$$T = \sum_i T_i = \sum_i \frac{\|\mathbf{s}_{rad,i}^H \mathbf{P}_{\tilde{\mathbf{H}}_i}^{\perp} \mathbf{y}_i\|^2}{(\mathbf{s}_{rad,i}^H \mathbf{P}_{\tilde{\mathbf{H}}_i}^{\perp} \mathbf{s}_{rad,i})(\mathbf{y}_i^H \mathbf{P}_{\tilde{\mathbf{H}}_i}^{\perp} \mathbf{y}_i)}. \qquad (19)$$

4. NUMERICAL EXAMPLES

To evaluate the performance of the proposed detector and compare two baseline methods that employ the all-one ("no BF") and Fourier-based beamforming patterns. In all simulations, we define the signal-to-noise ratio (SNR) and clutter-to-noise ratio (CNR) as

$$\text{SNR} = |\alpha|^2 (\mathbf{s}_{rad}^H \mathbf{s}_{rad})/\sigma^2, \qquad (20)$$

$$\text{CNR} = (\mathbf{c}^H \mathbf{H}^H \mathbf{H} \mathbf{c})/\sigma^2. \qquad (21)$$

In our setting, the number of beacon frames is $K = 16$ with the sector-level beam pattern given in the top plot of Fig. 2. The object is at $\theta = 20°$ while the clutter subspace is formed by $N_c = 6$ reflections uniformly sampled in $[-90°, 90°]$. We use two pairs of transmitting and receiving antenna number: $(M, N) = (16, 8)$ and $(M, N) = (32, 32)$. The detection performance is evaluated in terms of the receiver operating characteristic (ROC) by using Monte-Carlo trials.

We first consider a case of $(M, N) = (16, 8)$. In this case, the joint TX-RX antenna gains over three considered beam scanning schemes are shown in Fig. 3 (a). It is seen that Fourier-based

(a) TX-RX antenna gains (b) ROC
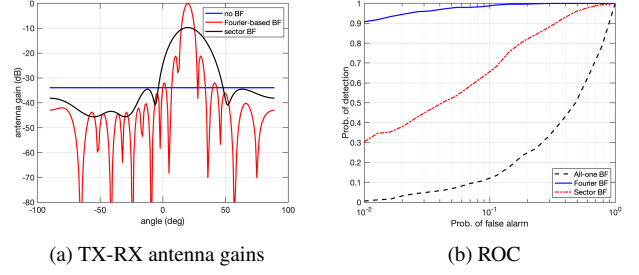
Fig. 3: Joint TX-RX antenna gains (a) and ROC curves when $(M, N) = (16, 8)$, SNR $= -20$ dB, and CNR $= 15$ dB.

(a) TX-RX antenna gains (b) ROC
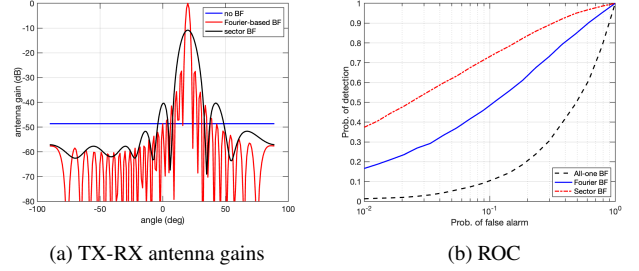
Fig. 4: Joint TX-RX antenna gains (a) and ROC curves when $(M, N) = (32, 32)$, SNR $= -20$ dB, and CNR $= 15$ dB.

beamforming can achieve the optimal antenna gain when its pointing direction is aligned with the object at $20°$. The sector-level beam scanning provides, in average, larger antenna gains than the Fourier-based one except at those angles close to the object. On the other hand, the all-one beam scanning provide no antenna gain over all directions. The corresponding ROC in Fig. 3 (b) shows that the Fourier-based one gives the best results while the sector-level beam scanning performs second. It is expected that, with a relatively small number of antennas, the Fourier-based beam scanning may still hit the object direction in high probability. If this happens, this results in a preamble sequence with an optimality-approaching SNR and leads to better detection performance than the sector-level beam scanning.

Next, we increase the number of TX and RX antennas to $(M, N) = (32, 32)$, the joint TX-RX antenna gain in Fig. 4 (a) becomes finer in the angle domain and larger mainlobe-sidelobe difference. Keeping the number of probing beacon frames the same, i.e., $K = 16$, the Fourier-based beam scanning has larger chances to "miss" the object within its mainlobe. The joint TX-RX antenna gain also reveals higher gain difference from the sector-level scanning to the all-one scanning. The corresponding ROC in Fig. 4 (b) confirms that the the sector-level beam scanning outperforms the Fourier-based scanning which provides sharper but may miss the object due to beam misalignment.

5. CONCLUSIONS

This paper considered DMG monostatic passive object detection with millimeter-wave (mmWave) Wi-Fi beacon frames. With an explicit signal model including preamble, antenna gains and clutter, we develop a GLRT detector that explores the Kronecker structure between the range steering vector and the Doppler steering vector. We further evaluate the impact of frame-to-frame antenna gains to the detection performance due to the beam scanning.

6. REFERENCES

[1] Rui Du, Hailiang Xie, Mengshi Hu, Narengerile, Yan Xin, Stephen McCann, Michael Montemurro, Tony Xiao Han, and Jie Xu, "An overview on IEEE 802.11bf: WLAN sensing," 2022.

[2] Cheng Chen, Hao Song, Qinghua Li, Francesca Meneghello, Francesco Restuccia, and Carlos Cordeiro, "Wi-Fi sensing based on IEEE 802.11bf," *IEEE Communications Magazine*, vol. 61, no. 1, pp. 121–127, 2023.

[3] Francesca Meneghello, Cheng Chen, Carlos Cordeiro, and Francesco Restuccia, "Toward integrated sensing and communications in IEEE 802.11bf Wi-Fi networks," *IEEE Communications Magazine*, vol. 61, no. 7, pp. 128–133, 2023.

[4] Steve Blandino, Tanguy Ropitault, Claudio R. C. M. da Silva, Anirudha Sahoo, and Nada Golmie, "IEEE 802.11bf DMG sensing: Enabling high-resolution mmWave Wi-Fi sensing," *IEEE Open Journal of Vehicular Technology*, vol. 4, pp. 342–355, 2023.

[5] P. Smulders, "Exploiting the 60 GHz band for local wireless multimedia access: prospects and future directions," *IEEE Communications Magazine*, vol. 40, no. 1, pp. 140–147, 2002.

[6] Hao Xu, V. Kukshya, and T.S. Rappaport, "Spatial and temporal characteristics of 60-GHz indoor channels," *IEEE Journal on Selected Areas in Communications*, vol. 20, no. 3, pp. 620–630, 2002.

[7] Thomas Nitsche et al., "IEEE 802.11ad: directional 60 GHz communication for multi-Gigabit-per-second Wi-Fi," *IEEE Communications Magazine*, vol. 52, no. 12, pp. 132–141, 2014.

[8] Yasaman Ghasempour et al., "IEEE 802.11ay: Next-generation 60 GHz communication for 100 Gb/s Wi-Fi," *IEEE Communications Magazine*, vol. 55, no. 12, pp. 186–192, 2017.

[9] Liangbin Li, Kaushik Josiam, and Rakesh Taori, "Feasibility study on full-duplex wireless millimeter-wave systems," in *2014 ICASSP*, 2014, pp. 2769–2773.

[10] Carlos Baquero Barneto, Sahan Damith Liyanaarachchi, Mikko Heino, Taneli Riihonen, and Mikko Valkama, "Full duplex radio/radar technology: The enabler for advanced joint communication and sensing," *IEEE Wireless Communications*, vol. 28, no. 1, pp. 82–88, 2021.

[11] Preeti Kumari, Nuria Gonzalez-Prelcic, and Robert W. Heath, "Investigating the IEEE 802.11ad standard for millimeter wave automotive radar," in *IEEE VTC2015-Fall)*, 2015, pp. 1–5.

[12] Preeti Kumari, Junil Choi, Nuria González-Prelcic, and Robert W. Heath, "IEEE 802.11ad-based radar: An approach to joint vehicular communication-radar system," *IEEE Transactions on Vehicular Technology*, vol. 67, no. 4, pp. 3012–3027, 2018.

[13] Gaurav Duggal, Shelly Vishwakarma, Kumar Vijay Mishra, and Shobha Sundar Ram, "Doppler-resilient 802.11ad-based ultrashort range automotive joint radar-communications system," *IEEE Transactions on Aerospace and Electronic Systems*, vol. 56, no. 5, pp. 4035–4048, 2020.

[14] Emanuele Grossi, Marco Lops, Luca Venturino, and Alessio Zappone, "Opportunistic radar in IEEE 802.11ad networks," *IEEE Transactions on Signal Processing*, vol. 66, no. 9, pp. 2441–2454, 2018.

[15] Emanuele Grossi, Marco Lops, and Luca Venturino, "Adaptive detection and localization exploiting the ieee 802.11ad standard," *IEEE Transactions on Wireless Communications*, vol. 19, no. 7, pp. 4394–4407, 2020.

[16] Emanuele Grossi, Marco Lops, Antonia Maria Tulino, and Luca Venturino, "Opportunistic sensing using mmwave communication signals: A subspace approach," *IEEE Transactions on Wireless Communications*, vol. 20, no. 7, pp. 4420–4434, 2021.

[17] Jian Wang, Jack Chuang, Samuel Berweger, Camillo Gentile, and Nada Golmie, "Towards opportunistic radar sensing using millimeter-wave Wi-Fi," *IEEE Internet of Things Journal*, pp. 1–1, 2023.